COBEM 2023 27TH INTERNATIONAL CONGRESS OF MECHANICAL ENGENEERING

ABCM Brazilian Society of Mechanical Sciences and Engineering
27th ABCM International Congress of Mechanical Engineering
December 04-08, 2023, Florianópolis-SC, Brazil

COB-2023-1354
NUMERICAL INVESTIGATION OF THE INTERMITTENT FLOW ONSET IN AN EVACUATED TUBE SOLAR COLLECTOR UNDER MULTIPLE OPERATING CONDITIONS

Fernando Claudio Spengler
Jacqueline Copetti
Nicolas Valmórbida
Mechanical Engineering Graduate Program
Universidade do Vale do Rio dos Sinos - Unisinos
fernandocspengler@gmail.com
jcopetti@unisinos.br
nicolasvalmorbida29@gmail.com

Abstract. *Heating systems that use evacuated tube solar collectors have proven to be more efficient than other solar heating systems. However, the performance of these systems can be hindered by certain operating conditions that result in fluid recirculation, which negatively impacts the heat transfer cycle inside the solar collectors. This issue can be exacerbated under extreme usage conditions, where water properties can amplify these unfavorable flows and lead to an intermittent flow regime inside the tubes. The heat transfer mechanisms involved in this type of solar collector were studied in this work using computational fluid dynamics. The numerical model is composed of the equations of conservation of mass, energy, and continuity and was validated based on the literature. The case study aimed to determine the transition point between the laminar and turbulent regimes in the internal flow of the evacuated tube, and this was achieved by varying the working temperature of the tube between 300K and 340K at three different inclination angles (30°, 45°, and 60°). The results of the study are presented in the form of velocity vectors, temperature contours, and mass flow rate profiles. The study identified the start of the turbulent regime in tubes inclined at 30°, 45°, and 60° as occurring between the operating temperatures of 330K and 340K, 310K and 315K, and 305K and 310K, respectively, for a heat transfer rate of 75W.*

Keywords: *solar collector, evacuated tube, computational fluid dynamics, inclination.*

1. INTRODUCTION

The acceleration of climate and environmental changes observed and described by the scientific community is directly related to the increase in energy demand and consumption. Since the Industrial Revolution, energy consumption has significantly increased due to technological progress and global socioeconomic development. The rising energy demand, coupled with the need for environmental preservation and the reduction of fossil fuel supply, calls for research and development of alternative energy sources (AGGARWAL et al., 2023).

Brazil has great potential for solar energy utilization. The use of solar energy provides a long-term positive return, as it enables the development of remote areas, regulates energy supply during dry periods, and reduces dependence on non-renewable sources (PEREIRA et al., 2006).

According to the Ministry of Mines and Energy (MME), water heating accounted for approximately 18% of electricity consumption in Brazilian households in 2018, representing 337 kWh per household. This value has been decreasing in relation to the absolute residential consumption, particularly due to the inclusion of solar heating systems (MME, 2020).

Vacuum tube solar water heating systems offer high performance compared to other water heating systems, with one of their main advantages being the isolation of the solar energy collection area by a vacuum. The water heated by solar radiation is isolated from the external environment by the vacuum, eliminating thermal conduction and convection, which considerably reduces heat losses from the system. This solution for water heating in residential buildings is becoming popular nationwide, highlighting the need for studies on its operation and performance. Experimental analysis of these heating systems is costly and sometimes unfeasible. However, computational numerical analysis provides a viable alternative. When the numerical method employed is accurate, the analysis yields result with minimal variation compared to experimental methods.

The convective processes that occur inside vacuum tube collectors allow for continuous fluid circulation, enabling the heating of large volumes, which are then stored in reservoirs. However, there are also flow patterns that do not favor the heat and mass transfer cycle, resulting in, among other things, fluid recirculation within the evacuated tube collectors.

More extreme usage conditions, such as increasing the water temperature at the tube inlet, amplify flow patterns that can be detrimental to system efficiency, leading to turbulent flow inside the tubes. While there are already numerous publications on the flow characteristics of vacuum tube collectors, there is a gap regarding the transition point from laminar to turbulent flow. Using computational fluid dynamics, this study aims to identify the operating temperature at which the flow in a sealed vacuum tube transitions to turbulent regime under different installation conditions.

2. METHODOLOGY

The study of flow behavior in a vacuum tube in this work was conducted using Computational Fluid Dynamics (CFD). The software modules ICEM-CFD, Fluent, and CFD-Post from ANSYS were employed. Following the parameters set by Budihardjo et al. (2007) for model validation, the simulations correspond to a single vacuum tube isolated from the thermal reservoir, as shown in Figure 1. The internal dimensions of the tube were based on the commercial model, with a length of L = 1.42 m and a diameter of d = 0.034 m.

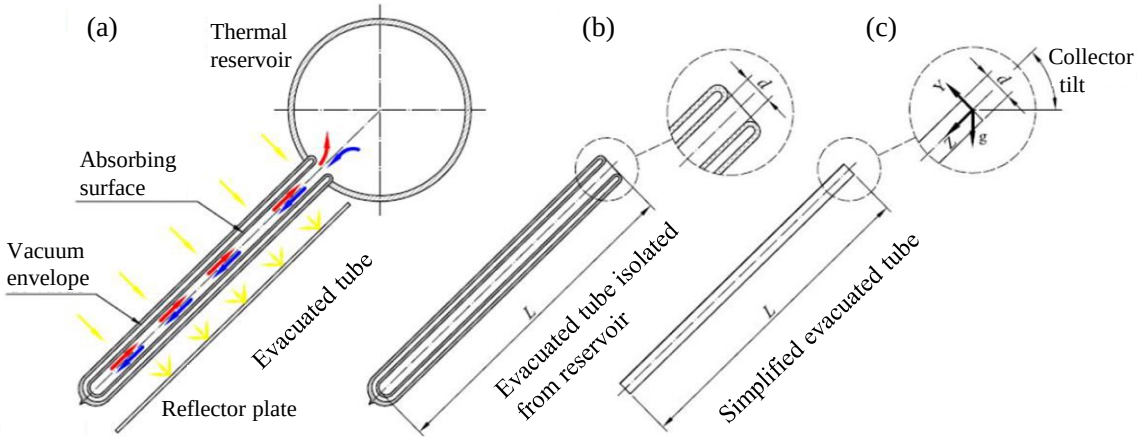

Figure 1 – Scheme adopted for the computational model: (a) evacuated tube, (b) evacuated tube isolated from the thermal reservoir, and (c) simplified evacuated tube. Source: Souza (2013).

2.1 Mathematical Model

In order to simulate the fluid dynamic processes occurring in evacuated tubes, an incompressible working fluid is considered, with constant thermophysical properties of water, and laminar flow regime. Therefore, the mathematical model consists of the continuity equation Eq. (1), Navier-Stokes equations Eq. (2-4), and energy equation Eq. (5), as presented below.

$$\frac{\partial u}{\partial x}+\frac{\partial v}{\partial y}+\frac{\partial w}{\partial z}=0 \tag{1}$$

$$\rho\left(\frac{\partial u}{\partial t}+u\frac{\partial u}{\partial x}+v\frac{\partial u}{\partial y}+w\frac{\partial u}{\partial z}\right)=-\frac{\partial p}{\partial x}+\mu\left(\frac{\partial^2 u}{\partial x^2}+\frac{\partial^2 u}{\partial y^2}+\frac{\partial^2 u}{\partial z^2}\right) \tag{2}$$

$$\rho\left(\frac{\partial v}{\partial t}+u\frac{\partial v}{\partial x}+v\frac{\partial v}{\partial y}+w\frac{\partial v}{\partial z}\right)=-\frac{\partial p}{\partial y}+\mu\left(\frac{\partial^2 v}{\partial x^2}+\frac{\partial^2 v}{\partial y^2}+\frac{\partial^2 v}{\partial z^2}\right)+\rho g \tag{3}$$

$$\rho\left(\frac{\partial w}{\partial t}+u\frac{\partial w}{\partial x}+v\frac{\partial w}{\partial y}+w\frac{\partial w}{\partial z}\right)=-\frac{\partial p}{\partial z}+\mu\left(\frac{\partial^2 w}{\partial x^2}+\frac{\partial^2 w}{\partial y^2}+\frac{\partial^2 w}{\partial z^2}\right) \tag{4}$$

$$\rho c_p\left(u\frac{\partial T}{\partial x}+v\frac{\partial T}{\partial y}+w\frac{\partial T}{\partial z}\right)=\kappa\left(\frac{\partial^2 T}{\partial x^2}+\frac{\partial^2 T}{\partial y^2}+\frac{\partial^2 T}{\partial z^2}\right) \tag{5}$$

Where u, v, and w are the velocity components in the x, y, and z directions, respectively, ρ represents the density, μ is the dynamic viscosity, k is the thermal conductivity, p denotes pressure, cp is the specific heat, and T represents temperature.

2.2 Initial, Boundary, and Operating Conditions

To identify the transition points of the flow regimes, twenty-one simulations were conducted, varying the inclination angle of the tube θ (30°, 45°, and 60°), as well as the operating temperature To, which varied from case to case. Additionally, the properties of water were varied according to Table 1.

Table 1 - Properties of water for the analyzed operating temperatures

To [K]	ρ [kg m^{-3}]	c_p [J kg^{-1} K^{-1}]	μ [Pa s]	k [W m^{-1} K^{-1}]	β [K^{-1}]
300	996.558	4180.6	0.00085074	0.61	0.00026586
305	995.077	4179.5	0.00076506	0.618	0.00031131
310	993.383	4179.2	0.00069361	0.626	0.00035479
315	991.495	4179.6	0.00063277	0.633	0.00039627
320	989.425	4180.5	0.00057972	0.64	0.00043577
330	984.787	4183.7	0.00049006	0.651	0.00050882
340	979.523	4188.5	0.00041907	0.661	0.00057394

The computational domain consists of three control surfaces: an inlet flat surface, a sealed flat surface, and a cylindrical surface, along with a symmetry plane. The sealed end of the tube is assumed to be adiabatic. The boundary condition on the cylindrical surface is a prescribed uniform heat transfer rate (q = 75 W), the same value used by Budihardjo (2007). Both surfaces are associated with the no-slip condition. On the inlet plane, which connects the tube to the reservoir, a free opening condition is specified, with a static pressure of 0 kPa and a constant absolute inlet temperature (*To*) that varies according to the studied case. The outlet temperature and mass flow rate vary according to the operating conditions. Regarding the simulation control conditions, an adaptive time-step was employed. For the convergence criteria, values of 10^{-3} were adopted for the velocity and continuity equations, and 10^{-6} for the energy equation. These conditions were used for numerical validation and subsequently for the case study.

Meshes with $11x10^5$, $8.4x10^5$, and $5.9x10^5$ elements (M1, M2, and M3, respectively) were tested. Regarding the mass flow rate, meshes M1 and M3 showed percentage errors of 1.0 and 1.7, respectively, compared to mesh M2. Therefore, the intermediate mesh (M2) was used for all simulations. The meshes are hexahedral, with refinement in regions with higher thermal and dynamic gradients in the system. The refined areas include the opening of the tube and its cylindrical surface, which define the domain boundary based on the boundary conditions of the problem (see Figure 1). Furthermore, considering that the boundary conditions of the case are axially symmetric, the mesh was developed considering a symmetry plane, reducing the total number of elements by half, and saving simulation time.

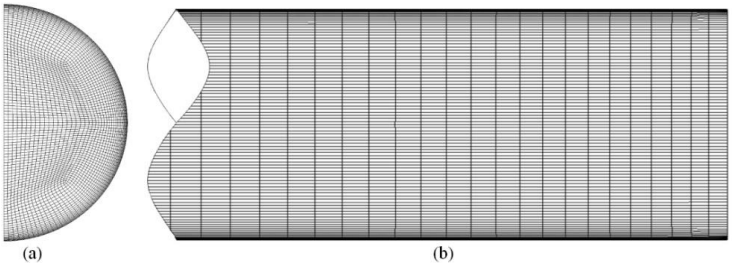

Figure 2 - Computational Mesh: (a) Cross-sectional view and (b) Longitudinal view

2.3 Post-processing

In addition to obtaining contours and vectors from the simulations in the post-processing software, data were collected for the calculation of dimensionless parameters. The Reynolds number of the flow at the open end was obtained using Eq. (6), where the mass flow rate ($\dot{m}$) from the simulation and the corresponding μ value at the operating temperature, as shown in Table 1, were used. The value obtained from Eq. (6) was compared with the correlation presented by Budihardjo et al. (2007) given by Eq. (7). Both results were plotted as a function of the Rayleigh number, given by Eq. (8).

$$Re = \frac{4\ \dot{m}}{\pi\ d\ \mu} \tag{6}$$

$$Re = a_0 \left[\frac{Nu\ Gr}{Pr} cos\ \theta \left(\frac{L}{d}\right)^{1,2}\right]^{a_1} \tag{7}$$

$$Ra = \frac{g\ \beta\ q\ \rho^2\ c_p}{\mu\ k^2}\ d^4 \tag{8}$$

where *Nu* is the Nusselt number ($Nu = hd/k$), *Gr* is the Grashof number ($Gr = \left[g\ \beta\ \left(T_p - T_\infty\right)\ d^3\ \rho^2\right]/\mu^2$), (related to the wall temperature T_p and the fluid temperature T_∞), *Pr* is the Prandtl number ($Pr = c_p\ \mu/k$), θ is the inclination angle of the tube, and gravity g = 9.81 m/s^2. The constants are: a_0 = 0.1914 and a_1 = 0.4048.

3. RESULTS

Firstly, the results of the numerical validation are presented, comparing them with those obtained by Budihardjo et al. (2007) in terms of velocity fields. Subsequently, the results of the internal flow behavior in the tube are presented, considering the variation of the inclination angle and the temperature increase. These results are presented in the form of velocity and temperature fields, as well as in terms of mass flow rate (ṁ) profiles as a function of time, and the behavior of dimensionless parameters with the variation of *To*.

3.1 Numerical Validation

Both quantitative (Figure 3) and qualitative (Figure 4) validation were performed using experimental results from Budihardjo et al. (2007). Figure 3 shows the profiles of the mass flow rate (ṁ) along the tube obtained from the present study and the referenced author. In this figure, a significant similarity between the results can be observed, with a maximum variation along the tube of 4%.

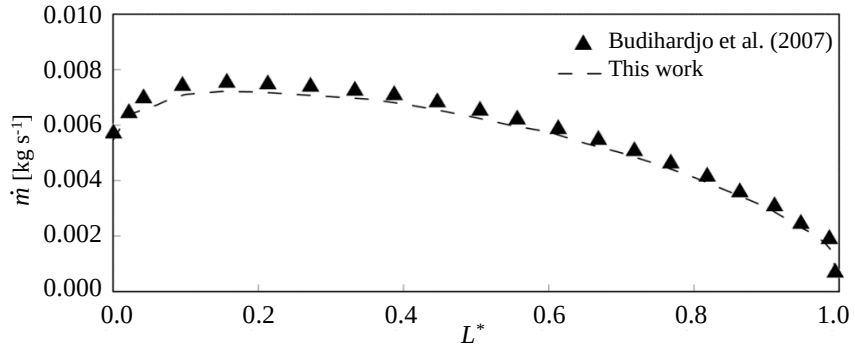

Figure 3 - Mass flow rate (ṁ) along the tube: Budihardjo et al. (2007) and present study.

In Figures 4(a, b), velocity fields are presented for four cross-sectional sections along the tube at L^* = 0, 1/4, 1/2, and 3/4, where L^* represents the dimensionless length of the tube. The fields correspond to the results obtained from the present study (Figure 4(a)) and those presented in the literature (Figure 4(b)).

In these figures, through the color scale, it can be observed that the velocity is zero throughout the contour of the tube, in accordance with the no-slip condition applied in the numerical model. The region of zero velocity observed in the middle of the cross-sectional sections identifies the shear region between the upward and downward flows, where the velocity is zero. It can also be observed that the velocity fields obtained in this study are like those presented by Budihardjo et al. (2007).

Based on the good quantitative and qualitative results presented in Figures 3 and 4, respectively, the mathematical and numerical model can be considered validated.

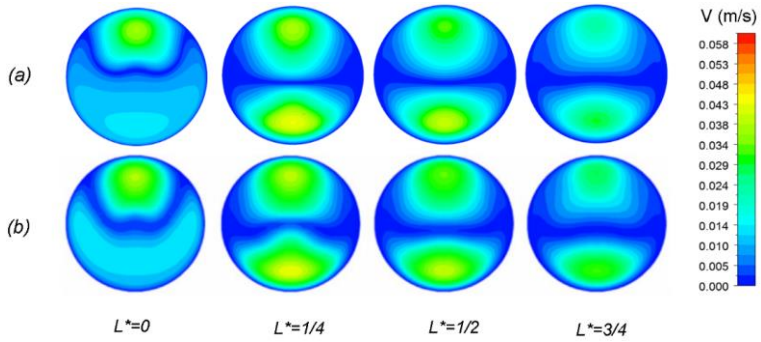

Figure 4 - Velocity contours: (a) present study; (b) Budihardjo et al. (2007).

3.2 Case Study

The following results correspond to a segment of the symmetry plane, delimited between the tube opening at $L^* = 0$ and a specific point along its length ($L^* = 0.20$), focusing on the evolution of the inlet and outlet flow behavior. This segment of the tube exhibited the greatest variations among the different cases, representing different flow patterns. The presented results are from the time instant $t = 150$ s, at which point the flows from all cases were already developed, as will be shown subsequently.

In Figures 5, 7, and 9, velocity vectors are presented, with the color gradient representing the variation of velocity (V) in the longitudinal plane for different values of *To*. On the other hand, Figures 6, 8, and 10 display temperature fields in the longitudinal section of the tube, with the color gradient representing the increase in temperature relative to *To* for each case. Although twenty-one cases were simulated, contours of temperature and velocity vectors for fifteen cases are presented, as the results were synthesized, omitting those that were visually similar to preceding simulations.

Regarding the velocity vectors in Figures 5, 7, and 9, it can be observed that the fluid velocity is zero at the walls, in accordance with the established boundary conditions. It is also noted that the velocity is zero near the center of the tube and throughout its length, separating the downward primary flow and the upward primary flow.

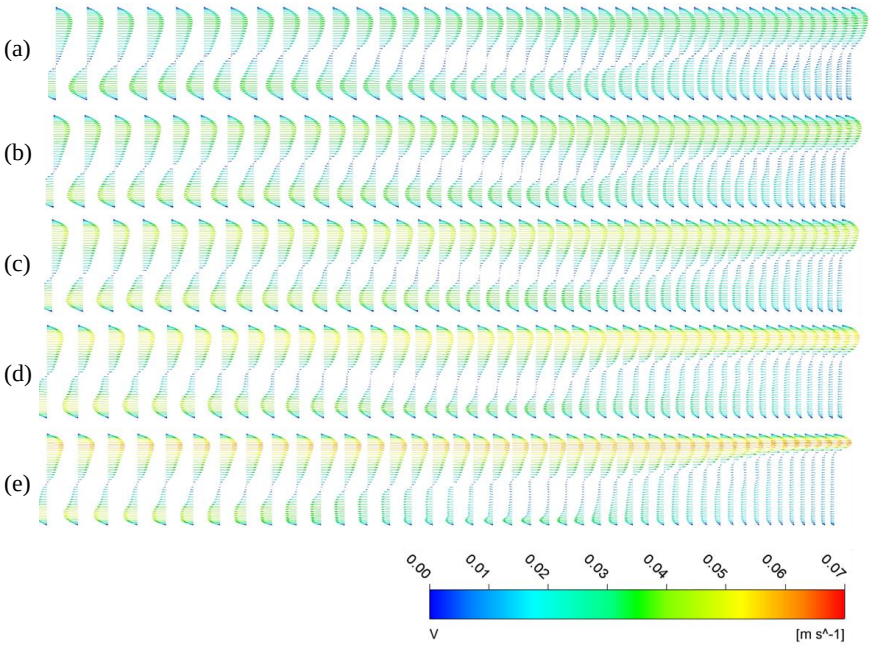

Figure 5 - Longitudinal velocity vectors for $\theta = 30°$: (a) *To* = 300 K; (b) *To* = 310 K; (c) *To* = 320 K; (d) *To* = 330 K; (e) *To* = 340 K.

Figures 5 and 6, related to velocity vectors and temperature fields for $\theta = 30°$, show well-defined flows and stratified temperature profiles for all values of *To*, characteristic of laminar flow. However, for the value of 340 K (Figure 6(e)), an

inconsistency is observed in the volume of unheated water entering the tube, indicating a slug of water restricting the exit area of the heated water.

The velocity vectors related to θ = 45° and *To* = 300 K and 310 K (Figure 7(a-b)) exhibit well-organized velocity profiles, which may indicate laminar behavior. However, as the temperature increases, progressively shown in these cases (Figure 7(c-e)), it is observed that the magnitude of the upward primary flow velocities, located in the upper zone of the tube, increases. Concurrently, in these figures, upward and downward flows are not as organized as in the previous cases. The shear zone becomes less evident, and contrary flows are observed at multiple levels. Recirculation zones are also noticed.

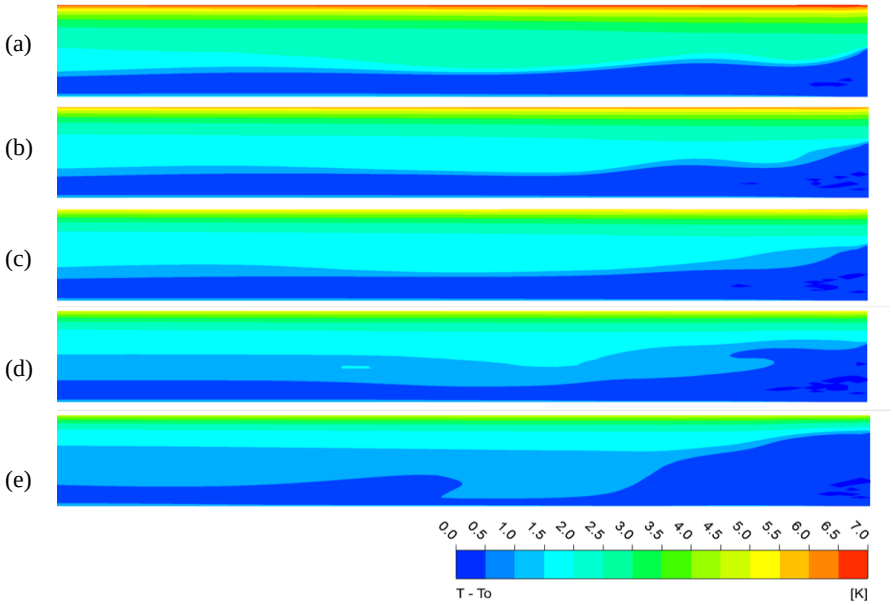

Figure 6 - Longitudinal temperature fields for θ = 30°: (a) *To* = 300 K; (b) *To* = 310 K; (c) *To* = 320 K; (d) *To* = 330 K; (e) *To* = 340 K.

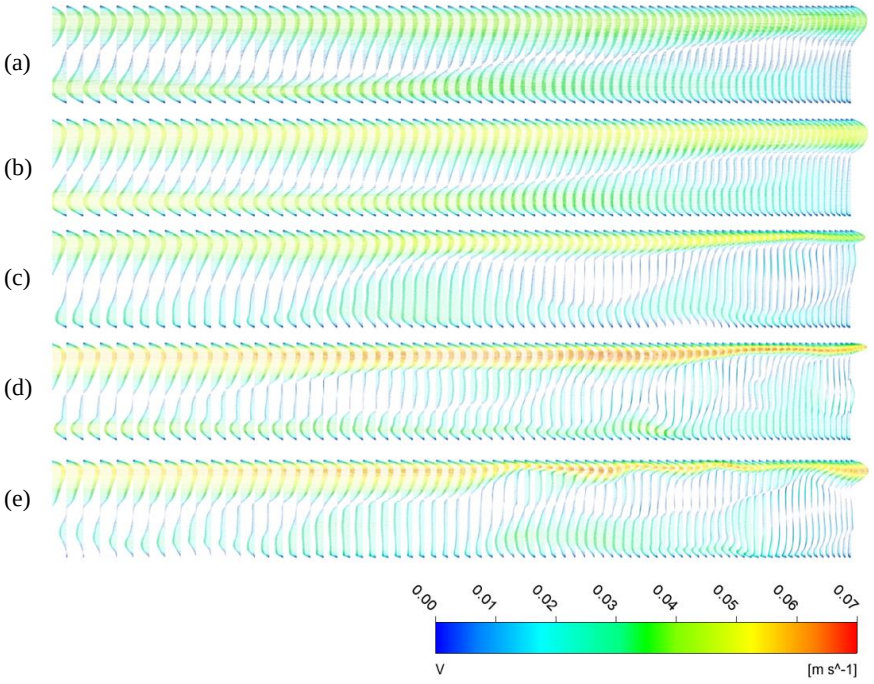

Figure 7 - Longitudinal velocity vectors for θ = 45°: (a) *To* = 300 K; (b) *To* = 310 K; (c) *To* = 315 K; (d) *To* = 320 K; (e) *To* = 330 K.

In Figures 8(a-b), a well-defined stratified flow is observed. In Figures 8(c-e), a stratified temperature behavior can still be observed, but it is less organized compared to the initial cases with lower temperatures.

For the angle $\theta = 60°$, the evolution of the described behavior occurs more rapidly, and from $To = 310$ K (Figure 9(b) and Figure 10(b)), intermittent flows entering the tube are observed, disrupting the upward and downward flows. The change from a well-defined stratified temperature field to an undefined one is related to the velocity vectors, and vice versa. For example, by analyzing the velocity vectors along with the temperature fields, it can be observed that in certain sections, the upward flow loses its characteristic due to disturbances generated by the downward flow. In this case, the incidence of water slugs entering the tube becomes evident.

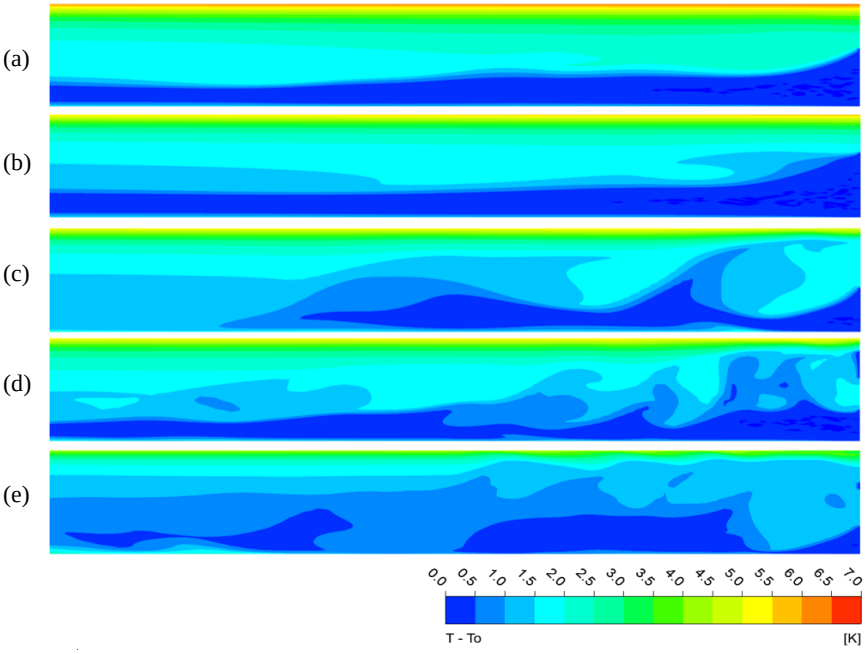

Figure 8 - Longitudinal temperature fields for $\theta = 45°$: (a) $To = 300$ K; (b) $To = 310$ K; (c) $To = 315$ K; (d) $To = 320$ K; (e) $To = 330$K.

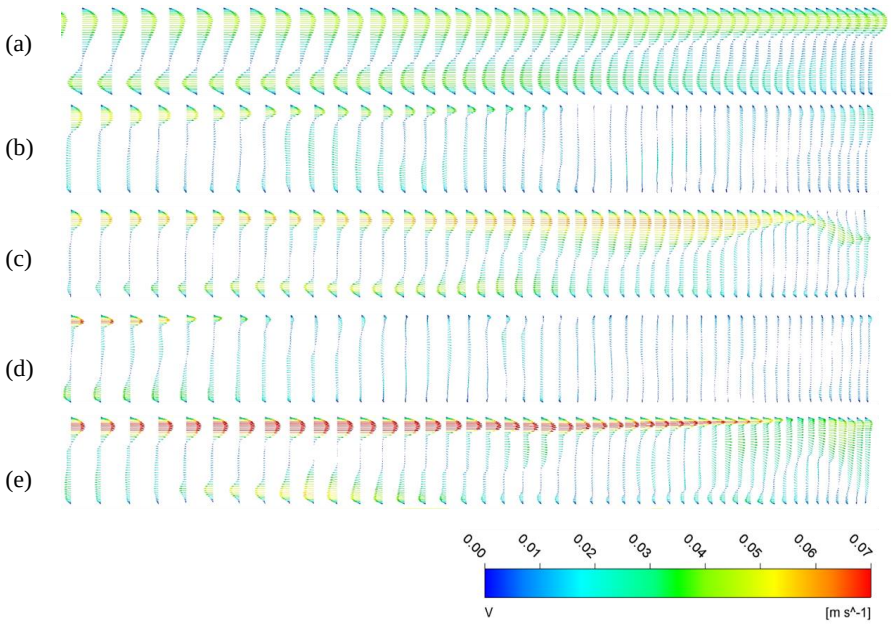

Figure 9 - Longitudinal velocity vectors for $\theta = 60°$: (a) $To = 300$ K; (b) $To = 310$ K; (c) $To = 320$ K; (d) $To = 330$ K; (e) $To = 340$ K.

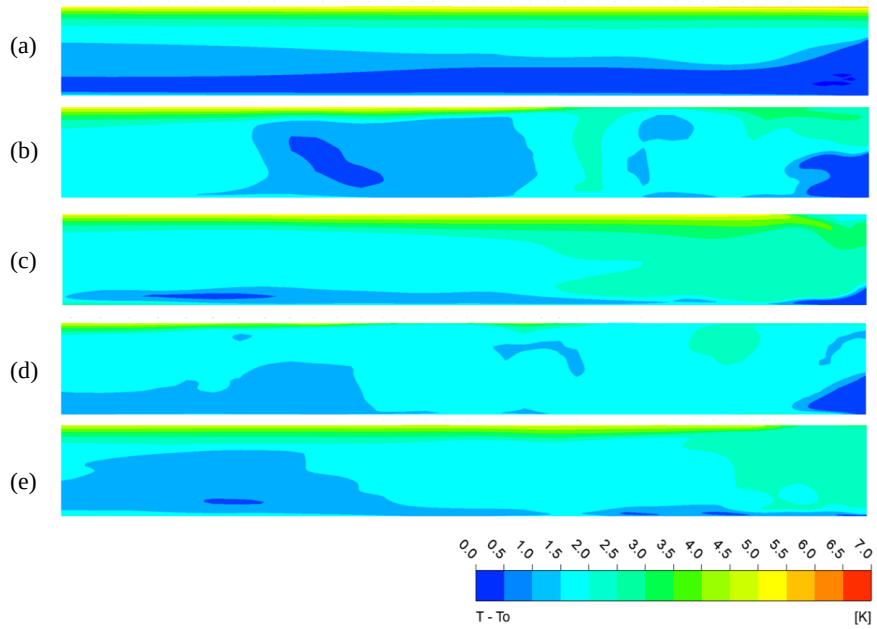

Figure 10 - Longitudinal temperature fields for θ = 60°: (a) *To* = 300 K; (b) *To* = 310 K; (c) *To* = 320 K; (d) *To* = 330K; (e) *To* = 340 K.

Figure 11 presents the mass flow rate profile over time for all the cases previously presented. It can be observed that increasing *To* and θ leads to an increase in the maximum value of ṁ and a reduction in the time t to reach the peak. This behavior can be explained by the increase in β and the decrease in μ with the increment of *To*, which amplify the buoyancy forces in the flow.

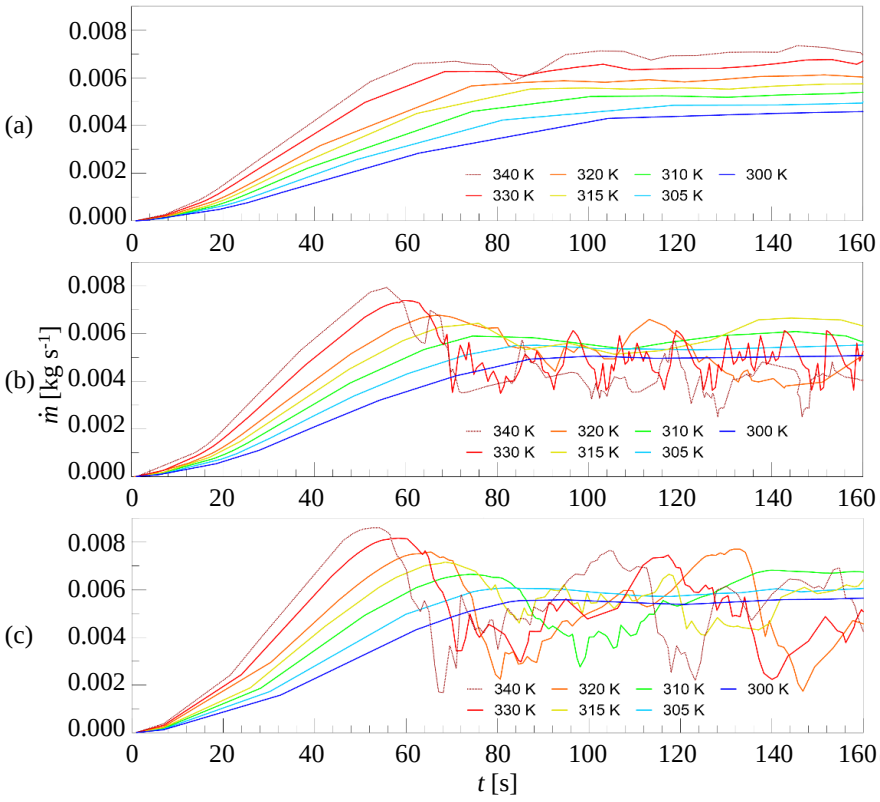

Figure 11 - Comparison of ṁ over time for different values of *To* according to the inclination angle of the tube: (a) θ = 30°; (b) θ = 45°; (c) θ = 60°.

The fluctuations observed in Figure 11 are due to the intermittency of water entering the tube, caused by the slug flow phenomena observed earlier. For all three angles θ, the behavior of ṁ after reaching its maximum value can be considered stable for *To* = 300 K. However, it is noticeable that as the angle θ increases, slug flow occurs at lower values of *To*. For θ = 30°, the intermittent mass flow begins to be observed at *To* = 340 K, while for θ = 45° and θ = 60°, this behavior starts at *To* = 315 K and *To* = 310 K, respectively. The oscillations in $\dot{m}$ following its maximum value amplify with increasing *To*, both in amplitude and frequency. Although the cases with higher *To* registered higher maximum $\dot{m}$ values, there is a decrease in the average $\dot{m}$ value in the subsequent time intervals.

Figure 12 presents Reynolds number profiles as a function of Rayleigh number for the three simulated angles θ. One profile was obtained using Eq. (6), with the average value of $\dot{m}$ over the cyclic or stable period presented in this work. The other profile was obtained based on values from Eq. (7) developed by Budihardjo et al. (2007). The points on the profiles correspond to the analyzed values of *To* in this study. By examining only the results from this study for each angle, it can be observed that for θ = 30°, Figure 12(a), there is a positive slope in the first six points corresponding to *To* = 300, 305, 310, 315, 320, and 330 K, followed by a decrease in the slope at *To* = 340 K. In Figure 12(b), corresponding to an angle θ = 45°, the slope changes direction from *To* = 315 K, while in Figure 12(c), corresponding to θ = 60°, the slope changes behavior at *To* = 310 K. These data reinforce the results and observations presented earlier, showing a correspondence between the change in slope of the graphs in Figure 11 and the transition to turbulent regime.

Comparing the results of this study with those obtained using the correlation by Budihardjo et al. (2007), there is agreement between them until the flow transitions to slug flow behavior. Therefore, the correlation is not consistent with the results from the turbulent regime onwards, and it is only applicable under laminar flow conditions.

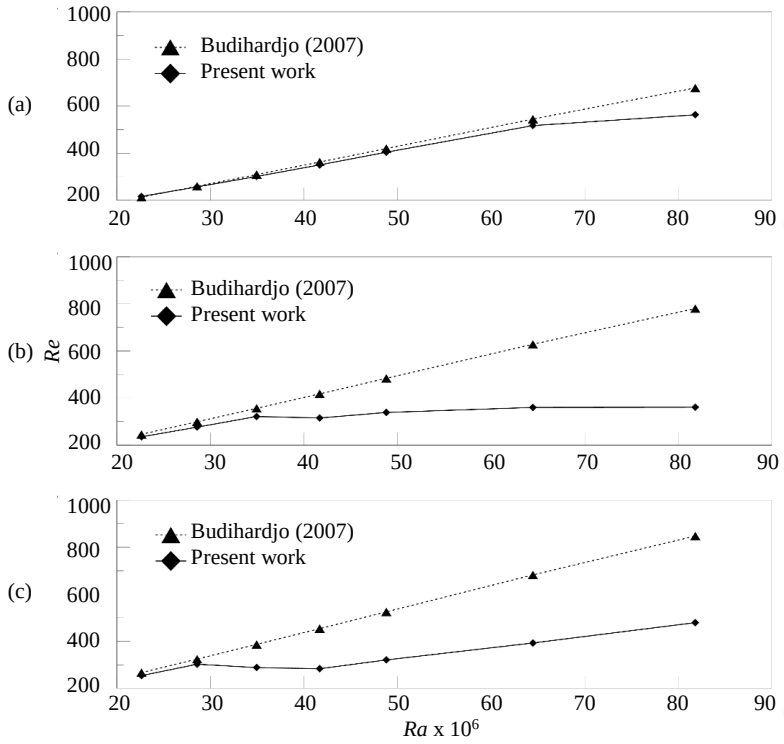

Figure 12 - Comparison between Re and Ra for data collected in the present study and the correlation established by Budihardjo et al. (2007) according to the inclination angle of the tube: (a) θ = 30°; (b) θ = 45°; (c) θ = 60°.

4. CONCLUSIONS

In this study, we investigated the transition from laminar to turbulent flow behavior in vacuum tubes under various operating conditions using computational numerical simulations. The results successfully validated our numerical model, affirming its reliability. We observed that the transition to the turbulent regime occurs at specific temperatures, depending on the tube's inclination angle. Furthermore, an increase in the tube's inclination angle reduces the transition temperature to the turbulent regime. This study provides valuable insights for the design and optimization of vacuum tube systems across various applications. We recommend future research to explore different operating conditions and mechanisms for mitigating the turbulent regime, as well as investigating the impact of intermittency on system thermal performance.

5. REFERENCES

AGGARWAL, S. et al. A comprehensive review of techniques for increasing the efficiency of evacuated tube solar collectors. HeliyonElsevier Ltd, , 1 abr. 2023.

Budihardjo, I., Morrison, G. L., Behnia, M., 2007. Natural circulation flow through water-in-glass evacuated tube solar collectors, Solar Energy, vol. 81, pp. 1460-1472.

MME., 2020. Consumo de Energia no Brasil – Análises Setororiais, Disponível em: <http://www.epe.gov.br/mercado/Documents/S%C3%A9rie%20Estudos%20de%20Energia/DEA%2020-14%20Consumo%20de%20Energia%20no%20Brasil.pdf> Acesso em: 15 Jan. 2023.

Pereira, E. B., Martins, F. R., Abreu, S. L., Rüther, R., 2006, Atlas brasileiro de energia solar, INPE, São José dos Campos, pp. 51-52.

Souza, F. R. O., 2013. Estudo numérico de características de escoamento e transferência de calor em coletor solar de tubo evacuado, Dissertação de mestrado, Universidade do Vale do Rio dos Sinos, São Leopoldo.

6. RESPONSIBILITY NOTICE

The authors are the only responsible for the printed material included in this paper.